Draft version July 23, 2021
Typeset using LaTeX **twocolumn** style in AASTeX631

A Search for Circumstellar Companions Around Nearby White Dwarf Sirius b

Miles Lucas [1], Michael Bottom [1], Garreth Ruane [2] and Sam Ragland [3]

[1] *Institute for Astronomy, University of Hawai'i, USA*
[2] *Jet Propulsion Laboratory, California Institute of Technology, USA*
[3] *W.M. Keck Observatory, USA*

ABSTRACT

1. INTRODUCTION

High-contrast imaging (HCI) is a powerful technique for discovering and characterizing exoplanets. Being able to probe the architecture, formation, and atmospheres of planets directly is necessary for advancing substellar companion formation and evolution theory. The process required to image a planet is daunting, however. The typical astrophysical flux ratios for a Sun-Jupiter analog in the near-infrared (NIR) are $\sim 10^{-8}$, and for a Sun-Earth system are $\sim 10^{-10}$ (Traub & Oppenheimer 2010). In addition, the close angular separation of planets makes it difficult to distinguish them from the diffraction pattern of the star and other noise sources. In order to make such a difficult detection it is imperative to minimize diffraction, scattering, and systematic noise.

Nearby white dwarfs (within ∼100 pc) are compelling targets for direct imaging searches, despite the limited knowledge of planetary systems around evolved stars. Burleigh et al. (2002) suggests planets on initially wide (¿5 AU) orbits around intermediate mass stars (1 $M_\odot$ to 8 $M_\odot$) will survive expansion during the red giant (RGB) phase and remain bound to the resultant white dwarf. During the asymptotic giant (AGB) phase, strong ionizing soft X-ray and UV emission will likely photoevaporate planetary atmospheres. In addition, the mass loss of the star will adiabatically expand the orbit of the planet by a maximum factor of $M_{*,\mathrm{WD}}/M_{*,\mathrm{MS}}$ (Jeans 1924).

Theoretical calculations show that planets can survive the red giant and asymptotic giant stages (Burleigh et al. 2002; Jura 2008; Nordhaus & Spiegel 2013), and results from radial velocity and transit surveys suggest extrasolar planets are prevalent throughout the Milky Way (Cumming et al. 2008).

However, only one planetary mass object has been detected around a white dwarf (WD) with imaging (WD 0806-661; Luhman et al. 2011).

Directly imaging exoplanets is a powerful method in exoplanet science which explores a parameter space very complementary to the popular transit photometry and radial velocity methods. The red giant stage has cleared planets within a few au greatly lowering the transit probability. White dwarfs have very few spectral lines to make high-precision radial velocity measurements from spectral lines. Imaging, though, benefits from the orbital expansion of the planet, and the cooling of the white dwarf greatly reduces the contrast between them (Burleigh et al. 2002; Gould & Kilic 2008). The Degenerate Objects around Degenerate Objects (DODO) survey observed 29 white dwarfs with Gemini/NIRI and VLT/ISAAC and provided upper limits around ∼8 M_J beyond 35 AU (Hogan et al. 2009).

In this work we study the closest white dwarf to the Sun, Sirius b, and provide upper mass limits based on our observations in the near-infrared. section 2 describes our target and observing strategy, section 3 describes the processing and analysis techniques used, section 4 describes our results and we conclude with section 5.

Sirius is one of the closest star system to the Sun at 2.7 pc away, consisting of an A1Vm star (a) and a WD with an age around 225 Myr (Bond et al. 2017; Collaboration et al. 2018). There are no known planets around either star, and using constrained 3-body numerical simulations a potential companion around Sirius b would only be stable with a 1.79 yr orbit, which corresponds to a circular orbit with 1.5 AU separation. Sirius b has been studied in the 10 µm regime recently by Pathak et al. (2021), who achieve 1.8 M_J to 3.5 M_J upper limits within 2 arcseconds.

2. OBSERVATIONS

Corresponding author: Miles Lucas
mdlucas@hawaii.edu

We targeted Sirius B directly using Keck/NIRC2 in Lp-band across three epochs in 2020 (Table 1). Our first attempt to observe Sirius B failed due to the strong scattered light from Sirius A. The adaptive optics (AO) calibration routinely failed when the extremely bright (-1.35 K-band magnitude) diffraction patterns would sweep into the field of view (FoV) of Sirius B (shown in Figure 1). Similarly, trying to deploy the focal-plane vortex coronagraph (Serabyn et al. 2017) failed when the low-order wavefront correction algorithm, QACITS (Huby et al. 2017), performed erratically in the presence of the scattered light. In order to overcome these issues, we decided to try using Sirius A as the NGS and off-axis guiding to Sirius B.

The Keck AO system (Wizinowich et al. 2000) was not designed to accomadate stars as bright as Sirius A, so we needed to attenuate the flux greatly to avoid saturating the wavefront sensor (WFS). We accomplished this using a narrow laser-line filter in front of the WFS, which brought Sirius A from $\sim$ -1.35 mag down to $\sim$ 5 mag. While still extremely bright, this was enough attenuation to close the AO loop. From here, we slewed off-axis using the separations and position angles calculated in Table 1 from the orbital parameters in Bond et al. (2017). In this mode, we noticed higher than usual drift in the focal plane, requiring manually recentering the target every 5 or 10 minutes. For both the November epochs we tried exploiting this by dithering between two positions in order to simplify background subtraction, but this ended up performing worse than the high-pass filter method we used in section 3. We tried deploying the vortex coronagraph along with QACITS, but again the scattered light from Sirius A made QACITS unstable, so we decided to forego any coronagraphy for the remaining observations.

During each observation, calibration frames were taken in the form of dark frames and sky flat frames. We also disabled the field rotator, which caused the FoV to rotate throughout the night for angular differential imaging (ADI; Marois et al. 2006).

3. ANALYSIS

For each epoch we applied a flat correction using calibration frames captured during observing. We also removed bad pixels using a combination of L.A.Cosmic (Dokkum & G 2001) and an adaptive sigma-clipping algorithm. We removed sky background using a high-pass median filter with a box size of 31 pixels. At this point frames were manually filtered to remove bad frames, especially those with diffraction spikes within a few hundred pixels, like in Figure 1. Then, each good frame is co-registered using cross-correlations (Guizar-Sicairos et al. 2008) as a first-order correction and then fitting each frame with a Gaussian PSF. The co-registered frames are then shifted to the center of the FoV. Lastly the frames were cropped to the inner 200 pixels and stacked into data cubes for each epoch. With the pixel scale of 10 mas/px the crop corresponds to a maximum separation of 1" or a projected separation of 2.7 AU. We also measure the parallactic angle of each frame, including corrections for distortion effects following Yelda et al. (2010). For each epoch, we measure the full-width at half-maximum (FWHM) of the stellar PSF by fitting a bivariate Gaussian model to the median frame from each data cube (an example of one is shown in Figure 2). All of the pre-processing code is available in Jupyter notebooks at the following GitHub repository[1] and the reduced data cubes and parallactic angles have been made available on Zenodo (Lucas et al. 2021).

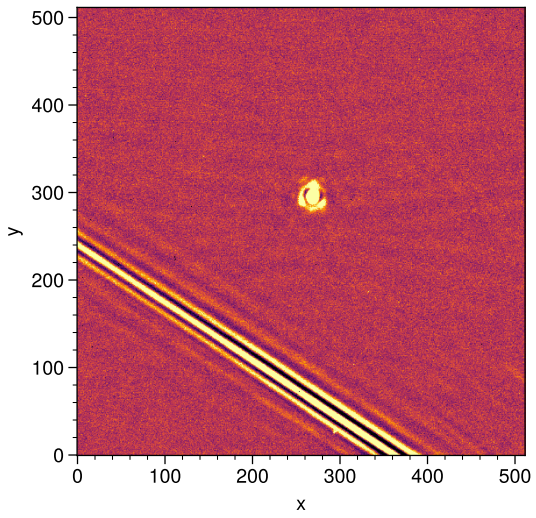

Figure 1. Calibrated science frame of Sirius b from 2020-02-04 epoch showing the strong scattered light effects from Sirius a.

By taking data with the field rotator disabled (ADI), the point-spread function (PSF), which is an instrumental effect, will not appear to rotate while any potential companion will appear to rotate. This allows modeling and subtracting the PSF with less probability for subtracting companion signal. After subtraction, the frames are derotated by their parallactic angle and combined with a weighted sum (Bottom et al. 2017), which reduces the pixel-to-pixel noise as the number of frames in the data cube increases.

[1] https://github.com/mileslucas/sirius-b

Table 1. Observing parameters for the three epochs of data. All observations were carried out using the NIRC2 Lp-band filter. Observation time is based on the frames that were selected for processing.

Date observed	Sirius A offset (arcsec)	Sirius A PA (°)	Observation time (hr)	FoV rotation (°)	FWHM (mas)	Seeing (arcsec)	Temp (°C)	PWV (mm)
2020-02-04	11.20	67.90	1.44	60.1	79.9			
2020-11-21	11.27	66.42	2.91	91.4	76.4			
2020-11-28	11.27	66.38	2.44	80.4	82.2			

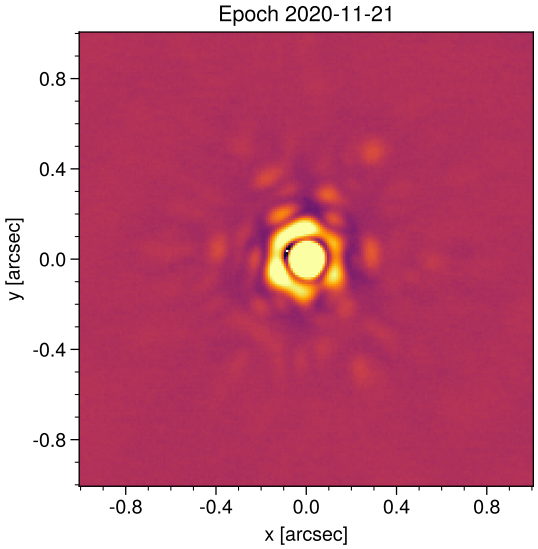

Figure 2. The median frame from the 2020-11-21 epoch showing the instrumental PSF. The inner core has a FWHM of ∼76 mas. The speckle pattern can be seen in the blobs surrounding the first ring, with roughly 6-way radial symmetry corresponding to the hexagonal shapes of the segmented mirrors.

For this analysis we used four statistical models for modeling the stellar PSF, classic median subtraction (Marois et al. 2006), principal component analysis (PCA; Soummer et al. 2012), non-negative matrix factorization (NMF; Ren et al. 2018), and fixed-point greedy disk subtraction (GreeDS; Pairet et al. 2019b, 2020). The median subtraction and PCA methods were also applied in an annular method, where we model the PSF in annuli of increasing separation frame-by-frame, discarding frames which have not rotated at least 0.5 FWHM (Marois et al. 2006).

We used three metrics for determining the performance of each algorithm, the signal-to-noise ratio (S/N) significance map, the standardized trajectory intensity mean map (STIM map; Pairet et al. 2019a), and the contrast curve. The significance and STIM maps assign a likelihood to each pixel for the presence of a companion using different assumptions of the residual statistics. The contrast curve determines the sensitivity of a 5σ statistical detection through repeated injection and retrieval of planetary signal as processed by one of the ADI algorithms above. We calculate both the Gaussian contrast and the Student-t corrected contrast, which accounts for the small-sample statistics in each annulus (Mawet et al. 2014). The collapsed residual frames along with the above metrics for each algorithm for each epoch can be found in Appendix A.

Another metric we explored was the STIM largest intensity mask map (SLIM map; Pairet 2020). The SLIM map is an ensemble statistic which calculates the average STIM map from many residual cubes along with the average mask of the N most intense pixels in each STIM map. We use the SLIM map with the PCA, NMF, and GreeDS algorithms because they all depend on choosing the number of basis components, which is hard to determine *a priori*. For each algorithm, we create residual cubes for increasing number of components, from 1 to 10. The collapsed residual frames, average STIM map, SLIM map, and contrast curves for each epoch for each of the above algorithms can be found in Appendix A. All of the code for these reductions can be found at the GitHub repository[2].

4. RESULTS

We determined the best-performing algorithms for each epoch using the contrast curves described in section 3. For the 2020-02-04 and 2020-11-21 epochs full-frame median subtraction had the best contrast at all separations. For the 2020-11-28 epoch annular PCA subtraction with 2 principal components and a rotation threshold of 0.5 FWHM produced the best contrast at close separations (0.5" to 1") and had similar performance to other algorithms beyond 1". The collapsed residual frames from each epoch are shown in Figure 3, along with the Gaussian significance maps (Figure 4) and STIM maps (Figure 5).

In these images there is not *consistent* or overwhelming evidence for a substellar companion. The STIM probability maps for the 2020-11-21 and 2020-11-28

[2] https://github.com/mileslucas/sirius-b

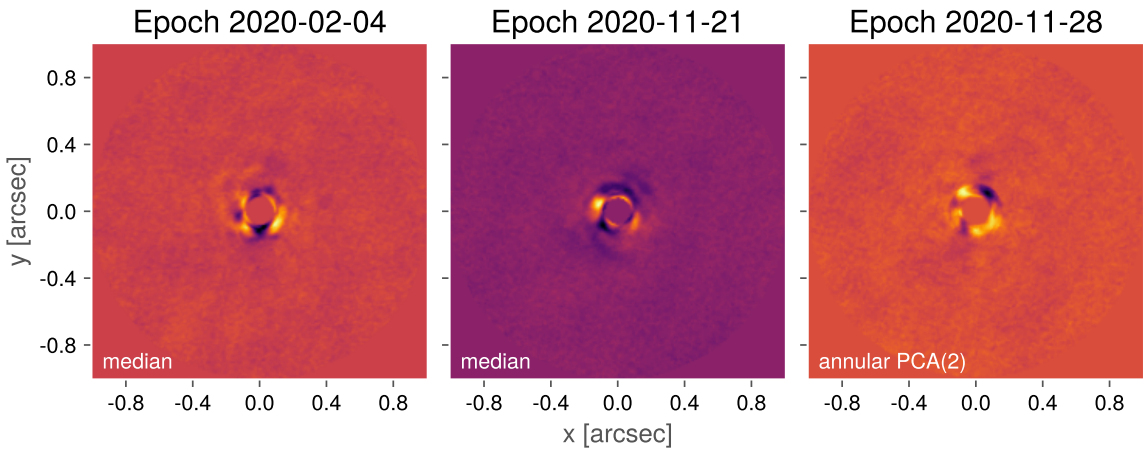

Figure 3. The flat residuals of each epoch after PSF subtraction, derotating, and collapsing. The inner full-width at half-maximum (FWHM) is masked out for each frame.

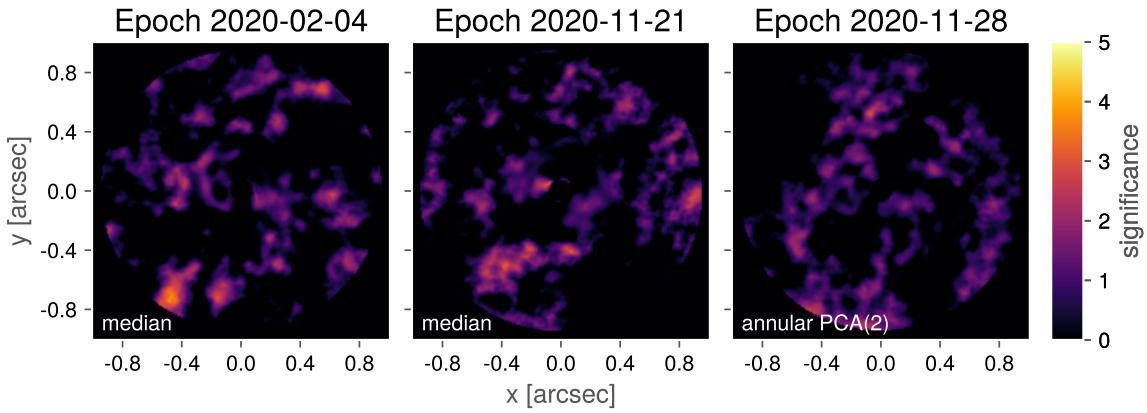

Figure 4. The *significance* maps for each epoch accounting for small sample statistics (Mawet et al. 2014). Typically a critical value for detection is 5. The inner full-width at half-maximum (FWHM) is masked out for each map.

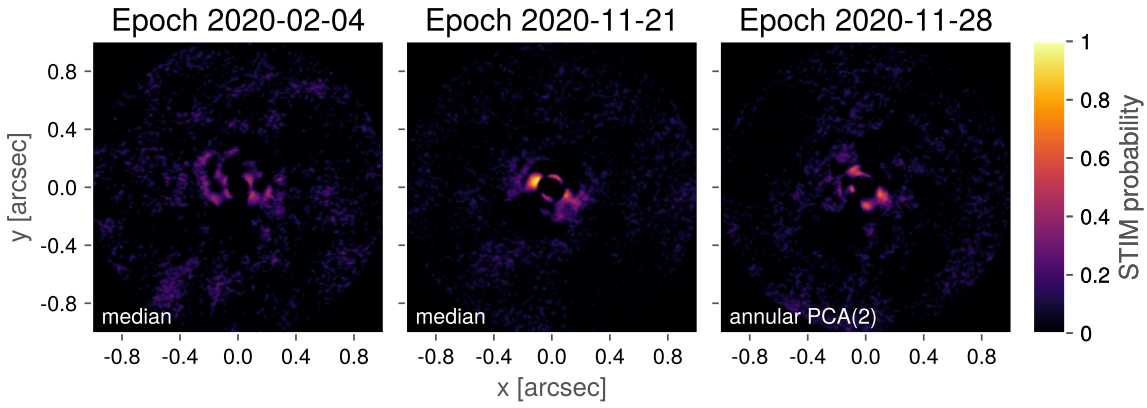

Figure 5. The STIM maps for each epoch calculated from the residual cube. Note that the STIM probability has a typical cutoff threshold of 0.5 for significant detections. The inner full-width at half-maximum (FWHM) is masked out for each map.

epochs suggest evidence for some blobs ∼0.13" from the center. The lack of evidence in the February epoch and the significance maps as well as the proximity to the central star (∼2 FWHM) all discredit the probability of these blobs being companions. Nonetheless, we estimated astrometry for blobs from each epoch (Table 2) and tried fitting Keplerian orbits using the "Orbits for the Impatient" algorithm (OFTI; Blunt et al. 2017). We generated 10^4 orbits, none of which managed to contain the points from each epoch (Appendix B). We take this as direct evidence against the blobs being substellar companions of any kind.

The contrast maps from the best performing algorithm for each reduction are shown in Figure 6. We determine the limiting sensitivities in terms of the planetary mass by first calculating the contrast-limited magnitude using an Lp-band magnitude for Sirius B of 9.1 (adapted from Bonnet-Bidaud & Pantin 2008). Then we use an age of 225 Myr to interpolate the planetary mass using the AMES-Cond evolutionary grid and atmosphere models (Allard et al. 2012). The best performing epoch was the 2020-11-21 night, which managed to reach an exceptional sensitivity of 3.5, 1.9, 1.1, 0.72 and 0.63 M_J at projected separations of 0.25, 0.5, 0.75, 1 and 2 AU (0.09, 0.19, 0.28, 0.38 and 0.75") respectively.

5. CONCLUSIONS

It is interesting to note that there is a symmetric shape in the residual frames from GreeDS and NMF for the November epochs. Both these algorithms were designed for imaging disks, so it is natural to consider this structure to be some kind of circumstellar debris disk.

Software: ADI.jl (Lucas & Bottom 2020), astropy (Collaboration et al. 2013; Astropy Collaboration et al. 2018), Julia (Bezanson et al. 2017), numpy (Harris et al. 2020), scikit-image (Walt et al. 2014),

REFERENCES

Allard, F., Homeier, D., & Freytag, B. 2012, Philos Trans A Math Phys Eng Sci, 370, 2765, doi: 10.1098/rsta.2011.0269

Astropy Collaboration, Price-Whelan, A. M., Sipőcz, B. M., et al. 2018, The Astronomical Journal, 156, 123, doi: 10.3847/1538-3881/aabc4f

Bezanson, J., Edelman, A., Karpinski, S., & Shah, V. B. 2017, SIAM Rev., 59, 65, doi: 10.1137/141000671

Blunt, S., Nielsen, E. L., De Rosa, R. J., et al. 2017, The Astronomical Journal, 153, 229, doi: 10.3847/1538-3881/aa6930

Bond, H. E., Schaefer, G. H., Gilliland, R. L., et al. 2017, The Astrophysical Journal, 840, 70, doi: 10.3847/1538-4357/aa6af8

Bonnet-Bidaud, J.-M., & Pantin, E. 2008, A&A, 489, 651, doi: 10.1051/0004-6361:20078937

Bottom, M., Ruane, G., & Mawet, D. 2017, Research Notes of the American Astronomical Society, 1, 30, doi: 10.3847/2515-5172/aa9d18

Burleigh, M. R., Clarke, F. J., & Hodgkin, S. T. 2002, Monthly Notices of the Royal Astronomical Society, 331, L41, doi: 10.1046/j.1365-8711.2002.05417.x

Collaboration, A., Robitaille, T. P., Tollerud, E. J., et al. 2013, Astronomy and Astrophysics, 558, A33, doi: 10.1051/0004-6361/201322068

Collaboration, G., Brown, A. G. A., Vallenari, A., et al. 2018, Astronomy & Astrophysics, Volume 616, id.A1, <NUMPAGES>22</NUMPAGES> pp., 616, A1, doi: 10.1051/0004-6361/201833051

Cumming, A., Butler, R. P., Marcy, G. W., et al. 2008, Publications of the Astronomical Society of the Pacific, 120, 531, doi: 10.1086/588487

Dokkum, V., & G, P. 2001, Publications of the Astronomical Society of the Pacific, 113, 1420, doi: 10.1086/323894

Gould, A., & Kilic, M. 2008, The Astrophysical Journal, 673, L75, doi: 10.1086/527476

Guizar-Sicairos, M., Thurman, S. T., & Fienup, J. R. 2008, Opt. Lett., OL, 33, 156, doi: 10.1364/OL.33.000156

Harris, C. R., Millman, K. J., van der Walt, S. J., et al. 2020, Nature, 585, 357, doi: 10.1038/s41586-020-2649-2

Hogan, E., Burleigh, M. R., & Clarke, F. J. 2009, Monthly Notices of the Royal Astronomical Society, 396, 2074, doi: 10.1111/j.1365-2966.2009.14565.x

Huby, E., Baudoz, P., Mawet, D., & Absil, O. 2017, The Astronomical Journal, 153, 43, doi: 10.3847/1538-3881/153/1/43

Jeans, J. H. 1924, Monthly Notices of the Royal Astronomical Society, 85, 2, doi: 10.1093/mnras/85.1.2

Jura, M. 2008, The Astronomical Journal, 135, 1785, doi: 10.1088/0004-6256/135/5/1785

Lucas, M., & Bottom, M. 2020, Journal of Open Source Software, 5, 2843, doi: 10.21105/joss.02843

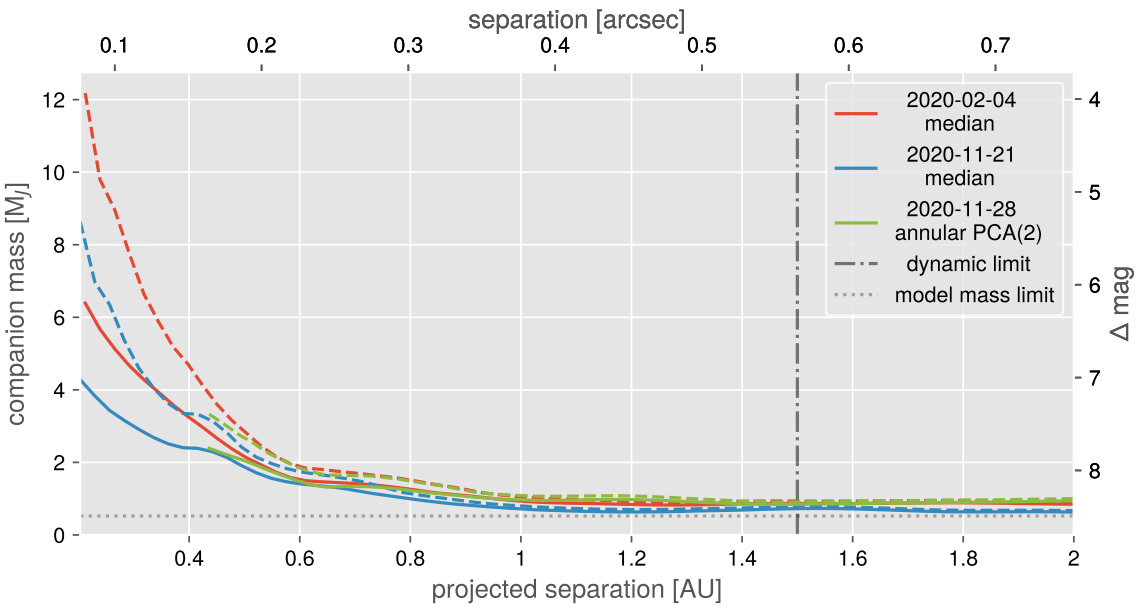

Figure 6. The contrast curves for the best performing algorithm from each epoch. The solid lines are the Gaussian 5σ contrast curves and the dashed lines are the Student-t corrected cuves (Mawet et al. 2014). In addition, the expected upper limit for orbital separation of a stable orbit (Bond et al. 2017) of 1.5 AU are plotted in a vertical dashed line. The companion mass values are interpolated from the AMES-Cond grid (Allard et al. 2012). The lower mass limit (upper magnitude limit) of these models is plotted in a light-gray horizontal dashed line.

Lucas, M., Bottom, M., Ruane, G., & Ragland, S. 2021, NIRC2 Sirius b ADI data, Zenodo, doi: 10.5281/zenodo.5115225

Luhman, K. L., Burgasser, A. J., & Bochanski, J. J. 2011, The Astrophysical Journal, 730, L9, doi: 10.1088/2041-8205/730/1/L9

Marois, C., Lafrenière, D., Doyon, R., Macintosh, B., & Nadeau, D. 2006, The Astrophysical Journal, 641, 556, doi: 10.1086/500401

Mawet, D., Milli, J., Wahhaj, Z., et al. 2014, ApJ, 792, 97, doi: 10.1088/0004-637X/792/2/97

Nordhaus, J., & Spiegel, D. S. 2013, Monthly Notices of the Royal Astronomical Society, 432, 500, doi: 10.1093/mnras/stt569

Pairet, B. 2020, PhD thesis, UCL - Université Catholique de Louvain. https://dial.uclouvain.be/pr/boreal/object/boreal:240621

Pairet, B., Cantalloube, F., Gomez Gonzalez, C. A., Absil, O., & Jacques, L. 2019a, Monthly Notices of the Royal Astronomical Society, 487, 2262, doi: 10.1093/mnras/stz1350

Pairet, B., Cantalloube, F., & Jacques, L. 2019b, arXiv:1812.01333 [astro-ph]. http://arxiv.org/abs/1812.01333

—. 2020, arXiv:2008.05170 [astro-ph]. http://arxiv.org/abs/2008.05170

Pathak, P., de la Roche, D. J. M. P. d., Kasper, M., et al. 2021, arXiv:2104.13032 [astro-ph]. http://arxiv.org/abs/2104.13032

Ren, B., Pueyo, L., Zhu, G. B., Debes, J., & Duchêne, G. 2018, The Astrophysical Journal, 852, 104, doi: 10.3847/1538-4357/aaa1f2

Serabyn, E., Huby, E., Matthews, K., et al. 2017, The Astronomical Journal, 153, 43, doi: 10.3847/1538-3881/153/1/43

Soummer, R., Pueyo, L., & Larkin, J. 2012, The Astrophysical Journal Letters, 755, L28, doi: 10.1088/2041-8205/755/2/L28

Traub, W. A., & Oppenheimer, B. R. 2010, Exoplanets, 111. http://adsabs.harvard.edu/abs/2010exop.book..111T

Walt, S. v. d., Schönberger, J. L., Nunez-Iglesias, J., et al. 2014, PeerJ, 2, e453, doi: 10.7717/peerj.453

Wizinowich, P. L., Acton, D. S., Lai, O., et al. 2000, 4007, 2, doi: 10.1117/12.390368

Yelda, S., Lu, J. R., Ghez, A. M., et al. 2010, The Astrophysical Journal, Volume 725, Issue 1, pp. 331-352 (2010)., 725, 331, doi: 10.1088/0004-637X/725/1/331

APPENDIX

A. ADI PROCESSING RESULTS

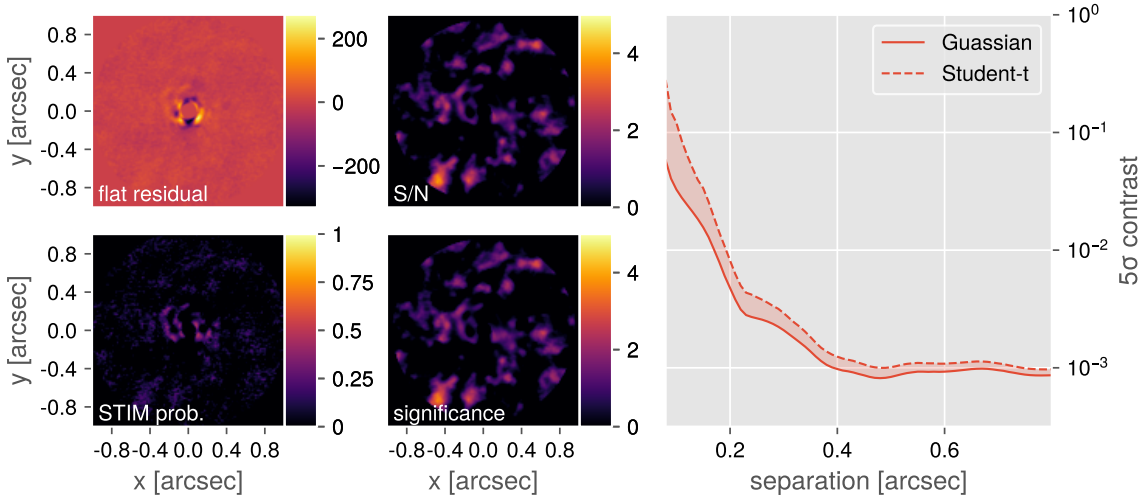

Figure 6. Results from processing each epoch of Sirius B data with various ADI algorithms. The top-left image is the subtracted, derotated, and collapsed image. The top-middle image is the Gaussian S/N map, the bottom-middle image is the Student-t S/N (significance) map, which typically requires a value of 5 to show a significant detection, and the bottom-left image is the STIM probability map, which typically requires a probability of 0.5 for significant detection. The right graph shows the 5σ contrast, both the Gaussian and Student-t corrected curves. The online figure set (21 images) contains the outputs for each algorithm tested on each epoch.

Fig. Set 6. ADI processing results

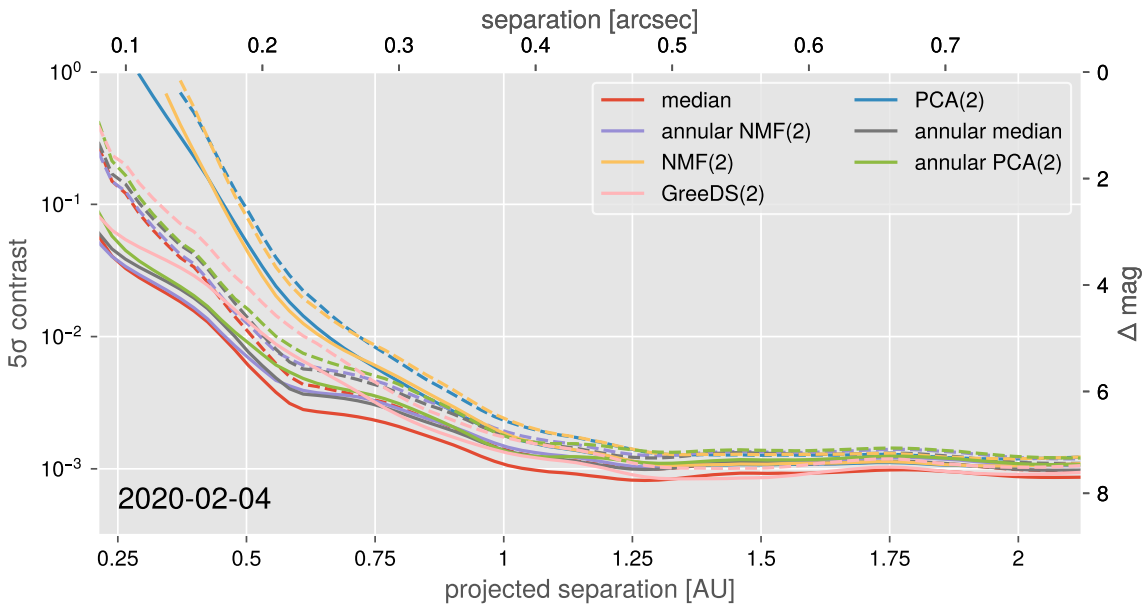

Figure 7. 5σ contrast curves from various ADI algorithms for the 2020-02-04 epoch. Both the Gaussian (solid lines) and Student-t corrected (dashed lines) contrast curves are shown.

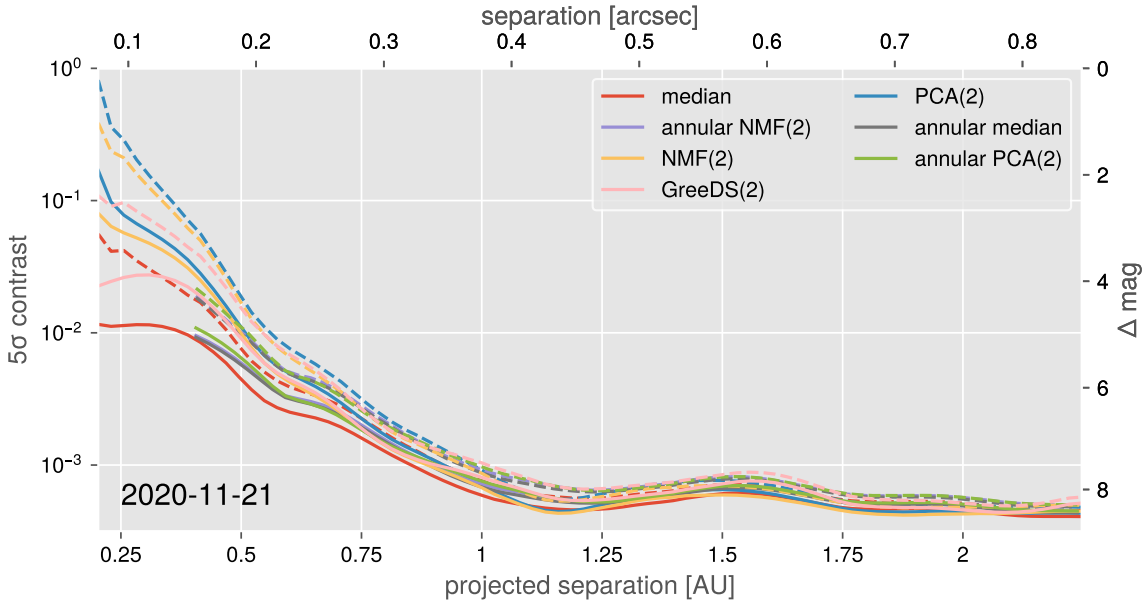

Figure 8. 5σ contrast curves from various ADI algorithms for the 2020-11-21 epoch. Both the Gaussian (solid lines) and Student-t corrected (dashed lines) contrast curves are shown.

B. PROVISIONAL ORBIT FITTING

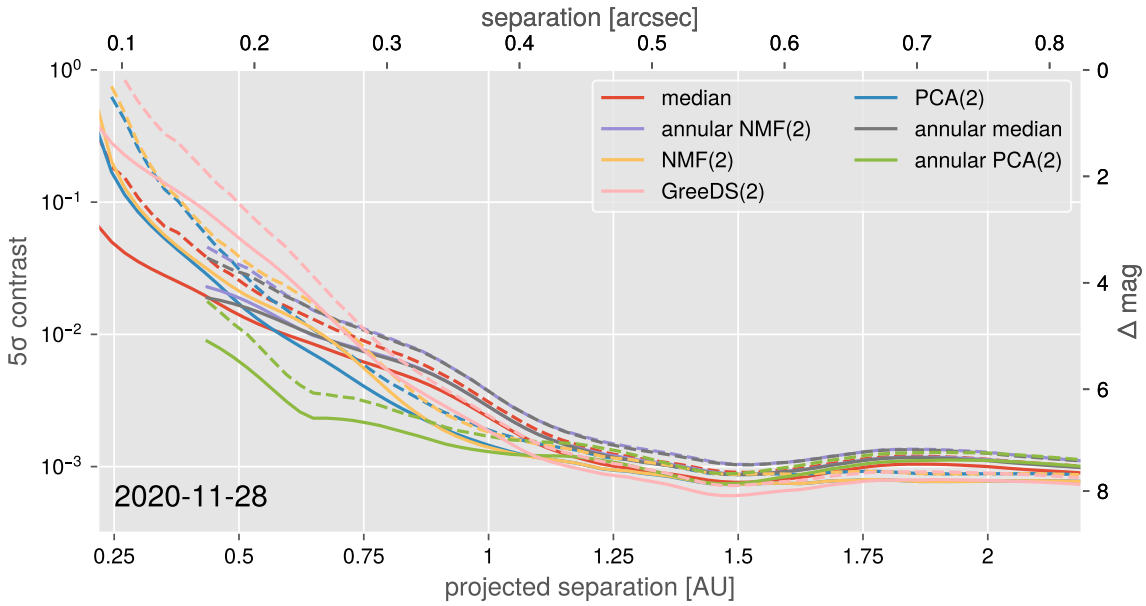

Figure 9. 5σ contrast curves from various ADI algorithms for the 2020-11-28 epoch. Both the Gaussian (solid lines) and Student-t corrected (dashed lines) contrast curves are shown.

Table 2. Provisional astrometry for blobs of interesest from each epoch. The uncertainties are represented in parantheses and are derived from the FWHM of the PSF from each epoch.

Date observed	offset (mas)	PA (°)
2020-02-04	193(38)	-99(11)
2020-11-21	125(38)	75(17)
2020-11-28	215(40)	23(11)

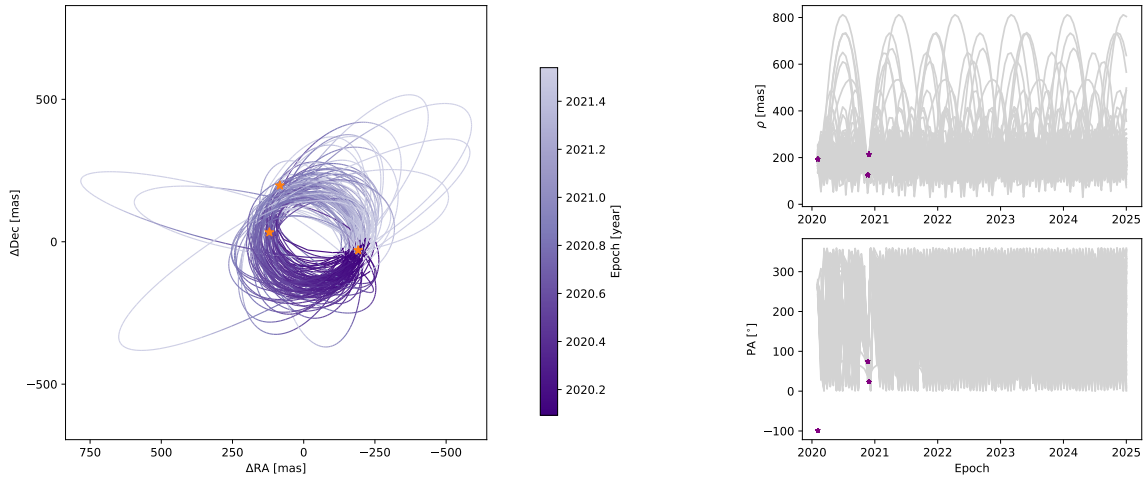

Figure 10. Provisional orbits fit using OFTI with 10^4 orbits. None of the orbits contain all three points within their uncertainties.